Simplified Resonant Parameter Design of the Asymmetrical *CLLC*-Type DC Transformer in the Renewable Energy System via Semi-Artificial Intelligent Optimal Scheme

Jingjing Huang, *Member, IEEE*, Xin Zhang, *Member, IEEE*, and Bin Zhao, *Member, IEEE*

***Abstract*—Asymmetrical *CLLC*-type dc transformers (ACLLC-type DCTs) are becoming more and more popular in the renewable energy system, thanks to the bidirectional power transmission (PT), high power density, and low-cost sensorless open-loop control. Nevertheless, the resonant frequency is not constant due to variations of the operation power and temperature in practice, which may make DCT lose its required voltage conversion gain and deteriorate the PT ability. This poses a challenge on the design of circuit parameters, especially when the open-loop scheme is usually recommended for the ACLLC-type DCT in the renewable energy system. Therefore, a semi-artificial intelligence (semi-AI)-based simplified parameter design approach is put forward in this paper for ACLLC-type DCT. It replaces all unknown parameters with two intermediate parameters through certain manipulations, and then utilizes a very simple computer-assisted procedure to optimally design the parameters of the ACLLC-type DCT. In addition, a detailed design example with a special planar transformer is presented via the aid of ANSYS Maxwell to achieve the desired resonant parameters of the ACLLC-type DCT. Finally, the proposed semi-AI-based method is experimentally demonstrated in a real renewable energy system prototype.**

***Index Terms*—CLLC, dc transformer (DCT), renewable energy system, parameter design, planar transformer.**

I. Introduction

CONVENTIONAL power market is dominated by ac systems on account of the historical reason that compared to dc voltage, ac voltage was easier to be regulated in olden days.

Manuscript received December 21, 2018; revised February 26, 2019 and May 3, 2019; accepted June 1, 2019. Date of publication June 11, 2019; date of current version November 12, 2019. This work was supported in part by the Academic Research Fund Tier 1 Grant RG 85/18 and in part by the Nanyang Technological University Start-Up Grant for Prof. X. Zhang. Recommended for publication by Associate Editor A. Safaee. *(Corresponding author: Xin Zhang.)*

J. Huang is with the Department of Electrical Engineering, Xi'an University of Technology, Xi'an 710048, China, and also with the School of Electrical and Electronic Engineering, Nanyang Technological University, Singapore 639798, Singapore (e-mail: hjj7759@163.com).

X. Zhang is with the School of Electrical and Electronic Engineering, Nanyang Technological University, Singapore 639798, Singapore (e-mail: jackzhang@ntu.edu.sg).

B. Zhao is with the Space Travelling-Wave Tube Research & Development Center, Institute of Electronics, Chinese Academy of Sciences, Beijing 100190, China, and also with the University of Chinese Academy of Sciences, Beijing 100049, China (e-mail: binzhao.iecas@foxmail.com).

Color versions of one or more of the figures in this paper are available online at http://ieeexplore.ieee.org.

Digital Object Identifier 10.1109/TPEL.2019.2922216

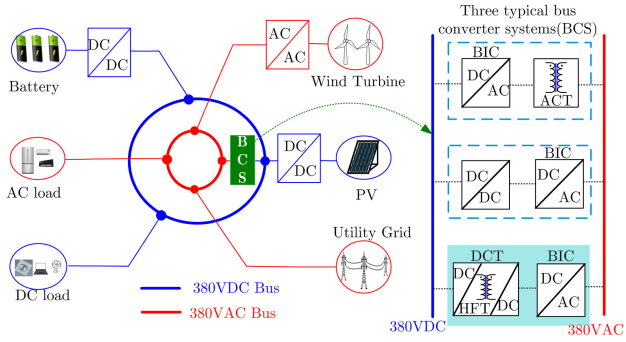

Fig. 1. Coexisting ac- and dc-type renewable energy system.

Nevertheless, in recent years, the dc-inherent energy storages, electronic loads, and renewable energy sources are increasing dramatically [1], [2]. Moreover, the developing power electronics make ac/dc, dc/ac, and dc/dc conversions possible. Therefore, the coexisting ac and dc power system comes up for the renewable energy system to reduce power conversions, improve energy efficiency, and enhance the compatibility [3], [4].

A coexisting ac- and dc-type renewable energy system is illustrated in Fig. 1. It can be used in low-power applications, such as emergency power supply, island without power, remote small villages, and so on. As depicted in Fig. 1, dc bus and ac bus are usually interlinked via a bus converter system (BCS) to optimize the renewable energy utilization. Since both dc and ac bus voltages are selected as 380 V to accommodate commonly used appliances at the user side [5], [6], three typical BCS topologies are available to link dc bus and ac bus: bidirectional interlinking ac/dc converter (BIC) + ac transformer [7]; dc/dc converter + BIC [8]; and dc transformer (DCT) + BIC [9].

Comparably, the BCS comprised of DCT + BIC is more competitive than the other two BCS topologies because it operates at high-frequency condition to improve the power density and save the space occupied [9]–[11]. Therefore, the focus of this paper is the DCT + BIC design in the renewable energy system.

BIC and DCT should cooperate with each other to transmit the power between ac bus and dc bus of the renewable energy system [10], [11]. In Fig. 2(a), V_H (V_L) and P_H (P_L), respectively, indicate the dc voltage and power in the high-voltage (HV) side

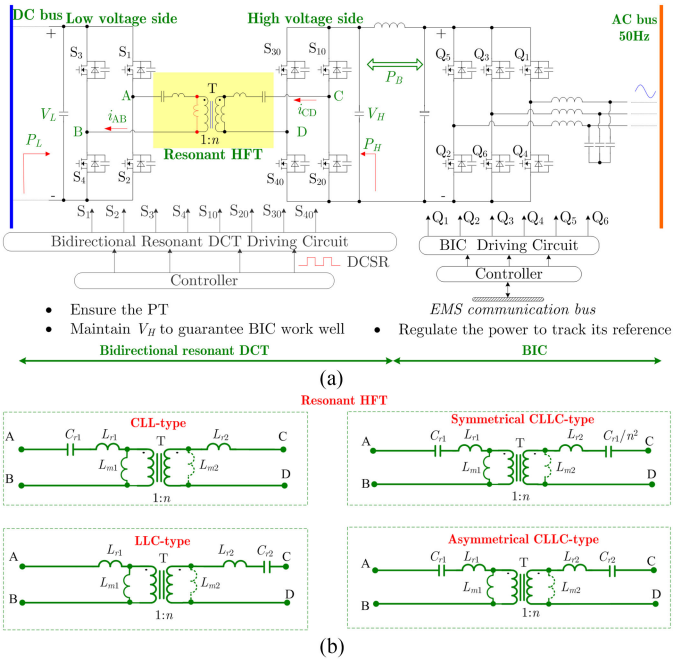

Fig. 2. (a) Topology of DCT and BIC. (b) Resonant HFT topologies.

(low-voltage (LV) side) of DCT. The way in which DCT and BIC cooperate is summarized as follows:

1) The transmitted power between ac bus and dc bus defined as P_B is fully regulated by BIC. Its reference $P_{B\text{ref}}$ is received from communication bus of energy management system (EMS) [12], [13]. As this technique is quite mature, it will not be further discussed in this paper.
2) DCT must realize two functions. One is to ensure P_B to cooperate with BIC. The other is to maintain HV voltage (V_H in Fig. 2(a)) within allowable range to guarantee the normal operation of BIC [14].

Frankly speaking, many dual-active-bridge (DAB) topologies are suitable for DCT application to transmit power bidirectionally [15], [16]. They can be classified as *CLL*-type, *LLC*-type, symmetrical *CLLC*-type, and asymmetrical *CLLC*-type based on the resonant high-frequency transformer (HFT) topology shown in Fig. 2(b) [17]–[20]. It is worthy to point out that the *CLL*-, *LLC*-, and symmetrical *CLLC*-type DAB actually can be considered as the special cases of the asymmetrical *CLLC*-type DAB, and all of them are suitable in the renewable energy system application [21]. In other words, if the engineer masters the design method of the asymmetrical *CLLC*-type DAB, he or she will naturally be skilled on the circuit design of *CLL*-, *LCC*-, and symmetrical *CLLC*-type DAB. Hence, the asymmetrical *CLLC*-type DAB is selected for DCT design here. For unifying the terminology, ACLLC-type DCT in introduced for asymmetric *CLLC*-type DAB based DCT.

For traditional applications [22], [23], the ACLLC-type DCT always operates as an independent conversion system with wide voltage conversion gain (VCG). Therefore, the closed-loop control is essential to adjust ACLLC-type DCT to its target voltage/power [24], which makes DCT very robust to the parameter variations. However, in the renewable energy system shown in Fig. 1, the ACLLC-type DCT must cooperate with the BIC instead of being an independent conversion system [10]. Because the transmitted power is controlled by BIC, and the potential stability problem of the DCT can be settled by regulating the equivalent impedance based on the relatively low-frequency BIC, the ACLLC-type DCT is recommended to operate with open-loop control to simplify systematic control and to reduce cost [21]. However, this poses a challenge on the ACLLC-type DCT circuit parameter design [25].

At present, there are two main parameter design methodologies that can be utilized to ensure both power transmission (PT) and VCG of ACLLC-type DCT. One is based on engineering experiences and mathematical derivations [19], [25]. Such kind of approach is suitable for the *CLL*-, *LLC*-, and systematical *CLLC*-type DCT, which can be simplified with only less than two unknown parameters, but it is hardly applied in the ACLLC-type DCT due to the increasing unknown coupled parameters. Another parameter design methodology is based on the artificial intelligence (AI) algorithm [26], which can find the optimum circuit parameters by comparing the predefined objective functions with the possible circuit parameters. Unfortunately, numerous unknown parameters of the ACLLC-type DCT also bring algorithm complexity and heavy calculation load by the AI algorithm. Note that both these parameter design methodologies hardly settle the issue induced by the practical values' changes of inductances and capacitances due to the model complexity and computational burden. In addition, how to optimally design the parameters of the ACLLC-type DCT with consideration of the aforementioned issues is also rarely reported.

Therefore, a semi-AI-based simplified circuit parameter design approach is proposed for ACLLC-type DCT of the renewable energy system in this paper to ensure PT ability and optimize VCG. Its main contributions are summarized as follows:

1) Considering the parameter variations, the challenge and design criteria of ACLLC-type DCT are refined from PT and VCG point of view to facilitate parameter design by transforming all unknown parameters to only two intermediate parameters.
2) According to the derived design criteria, the optimum resonant circuit parameter design procedure is proposed with the aid of semi-AI method. Meanwhile, an illustrative design example including a special planar transformer is also presented in detail with the help of ANSYS Maxwell to achieve the desired resonant parameters.
3) The proposed parameter design approach is experimentally verified via a renewable energy system prototype as well.

The rest of this paper is organized as follows: the design challenges of the ACLLC-type DCT are illustrated in Section II. In view of PT and VCG, the design criteria of the DCT are proposed in Section III to simplify the parameter design procedure. Subsequently, the semi-AI-based optimum resonant parameter design procedure and a design example are presented in Sections IV and V, respectively. Experimental verifications are illustrated in Section VI, and Section VII summarizes this paper.

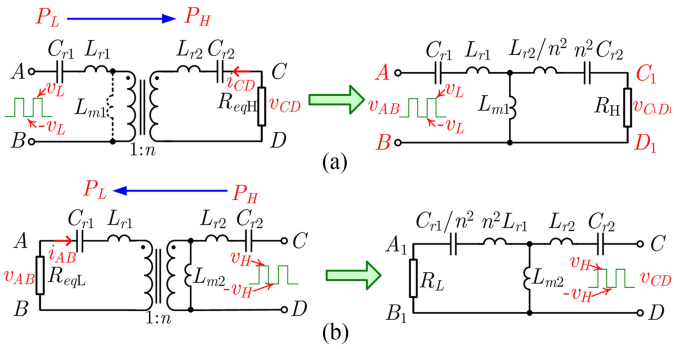

Fig. 3. Equivalent model of the ACLLC-HFT when power is transferred as (a) LV → HV and (b) HV → LV.

II. Design Challenges of the ACLLC-Type DCT

A. Parameters Need to Be Designed

According to Fig. 2(b), the key parameter design of ACLLC-type DCT mainly depends on ACLLC-type HFT (ACLLC-HFT). When power is transmitted bidirectionally, the equivalent ACLLC-HFT circuit diagrams are depicted in Fig. 3, whose circuit parameters are arranged as follows:

1) magnetizing inductances: L_{m1} and L_{m2};
2) leakage inductances: L_{r1} and L_{r2};
3) turn ratio: n;
4) series resonant capacitances: C_{r1} and C_{r2};
5) equivalent resistances: R_H and R_L [19]

$$R_H = \frac{R_{\mathrm{eq}H}}{n^2} = \frac{v_{\mathrm{CD}}}{n^2 i_{\mathrm{CD}}}|_{p_{L\to H}} = \frac{8V_H^2}{n^2\pi^2 P_H} \tag{1a}$$

$$R_L = n^2 R_{\mathrm{eq}L} = n^2 \frac{v_{\mathrm{AB}}}{i_{\mathrm{AB}}}|_{p_{H\to L}} = \frac{8n^2 V_L^2}{\pi^2 P_L} \tag{1b}$$

where $v_{\mathrm{CD(AB)}}$ and $i_{\mathrm{CD(AB)}}$ denote voltage and current at CD (AB) port, respectively.

B. Design Challenges

The actual values of inductances and capacitances are changing with power, temperature, etc. [29]. For convenience, the variable ranges of the actual inductances and capacitances are defined as follows:

$$L_x \in [(1-\zeta\%)L_{xR},\ (1+\zeta\%)L_{xR}] \tag{2a}$$

$$C_x \in [(1-\xi\%)C_{xR},\ (1+\xi\%)C_{xR}] \tag{2b}$$

where L_x and C_x represent L_{r1}, L_{r2}, L_{m1}, L_{m2}, and C_{r1} and C_{r2}, respectively; L_{xR} and C_{xR} are the designed values of L_x and C_x at the rated temperature and power; and $\zeta\%$ and $\xi\%$ are possible variable ranges of L_x and C_x, respectively, which are achieved based on the possible variations of power and temperature.

Based on (2), a reality issue comes up to ACLLC-type DCT: It is known that the changing inductances, capacitances, and power make the resonant frequency f_r vary online. However, the switching frequency f_s is constant in the 50% duty cycle based semiregulated (DCSR) open-loop control. Therefore, when the changing f_r deviates from the constant f_s, the inappropriate parameters may seriously degrade the PT and VCG of the ACLLC-type DCT.

Therefore, the DCSR control poses a challenge on the parameter design of DCT against the resonant parameter variations to guarantee the PT and VCG. It is noteworthy that good PT ability also indicates high efficiency.

C. Objective

To cope with the issue in Section II-B, the parameters must be appropriately designed against the parameter variations. However, as mentioned in the introduction, the existing design methods cannot fix the optimum inductances and capacitances when considering the parameter variations, especially with the increasing unknown parameters of ACLLC-type DCT. Therefore, a suitable parameter design approach is required to achieve the following two goals in the renewable energy system:

1) Ensure PT ability to naturally reduce the loss in entire power range.
2) Optimize VCG to offset parameter variations.

This is the objective of the present paper, which will be achieved by proposing a semi-AI-based robust resonant parameter design approach in the subsequent sections.

III. PT- and VCG-Oriented Design Criteria

To simplify the parameter design procedure, the design criteria of ACLLC-type DCT are presented in this section for renewable energy system application to realize the following:

1) Criterion I is utilized to ensure the satisfactory PT.
2) Criterion II is employed to optimize the VCG.

Meanwhile, all unknown parameters are transformed to two intermediate parameters, with the details elaborated further.

A. Design Criterion I to Ensure PT

1) Design Requirement Based on PT: In the following, to further facilitate the resonant parameter design, a series of intermediate design indices (ω_1, ω_{*1}, Q_1, g, k) are defined

$$\omega_1 = 1/\sqrt{L_{r1}C_{r1}} \tag{3a}$$

$$\omega_{*1} = \omega_s/\omega_1 \quad (\omega_s = 2\pi f_s) \tag{3b}$$

$$Q_1 = \sqrt{L_{r1}/C_{r1}}/R_H \tag{3c}$$

$$g = n^2 C_{r2}/C_{r1} \tag{3d}$$

$$k = L_{m1}/L_{r1} = L_{m2}/L_{r2}. \tag{3e}$$

The maximum PT depends on the relationship between f_s and f_r. Therefore, if ACLLC-type DCT is operating with open loop, the design requirement from maximum PT point of view is [25]

$$f_s = f_r. \tag{4}$$

2) Design Criterion From PT Point of View:

a) Power flow with LV → HV: When power is transmitted as LV → HV, as given in Fig. 3(a), the transfer function is

obtained as

$$G(j\omega_s)|_{\mathrm{LV}\to\mathrm{HV}} = \frac{u_{\mathrm{C1D1}}}{u_{\mathrm{AB}}} = \frac{\omega_s L_{m1} R_H}{[(\omega_s L_{r1} - 1/(\omega_s C_{r1}) + \omega_s L_{m1})R_H + jX_{\mathrm{eq}}]} \quad (5)$$

where $L_2 = L_{r2}/n^2$, $C_2 = n^2 C_{r2}$, and

$$X_{\mathrm{eq}} = 2\omega_s^2 L_{m1} L_{r1} + \omega_s^2 L_{r1}^2 - (L_{m1}/C_{r1}) - (L_{m1}/C_2) - (L_{r1}/C_2) - (L_2/C_{r1}) + (1/\omega_s^2 C_{r1} C_2).$$

To ensure the maximum PT, the DCT should operate at the resonant status. Thus, the imaginary term of (5) is zero; i.e., $X_{\mathrm{eq}} = 0$, which can be derived as

$$\omega_8^4 x - y\omega_8^2\omega_1^2 + z\omega_1^4 = 0 \quad (6)$$

where

$$x = 2k + 1 \quad (7a)$$

$$y = k + k/g + 1/g + 1 \quad (7b)$$

$$z = 1/g. \quad (7c)$$

Therefore, the resonant angular frequency defined as ω_r can be achieved as

$$\omega_r = \sqrt{(y \pm \sqrt{y^2 - 4xz})/(2x)}\,\omega_1. \quad (8)$$

Since the value of L_{m1} is much higher than L_{r1} in the designed DCT, DCT is thus operating with the series resonant angular frequency

$$\omega_r|_{\mathrm{LV}\to\mathrm{HV}} = f_{\omega_r}(k,g)\omega_1 \quad (9a)$$

$$f_{\omega_r}(k,g) \triangleq \sqrt{(y + \sqrt{y^2 - 4xz})/(2x)}. \quad (9b)$$

b) Power flow with HV → LV: In a similar way, when the power is transferred with HV → LV, as shown in Fig. 3(b), the series resonant angular frequency can be achieved, and thus not further discussed here.

c) Conclusion of design criterion I: Therefore, f_s should be adjusted as (9). As a result, to maximize PT, design criterion I is

$$f_s = \omega_{rR}/2\pi = f_{\omega_r}(k,g)\omega_1 \quad (10)$$

where ω_{rR} indicates the value of ω_r at the rated temperature and power.

B. Design Criterion II to Ensure VCG

1) Design Requirement Based on VCG: As mentioned in Fig. 2, V_L is kept by the dc subgrid. Practically, the fluctuation exists in V_L when cooperating with power dispatch method of EMS [30]. Therefore, the actual variable range of V_L is described as

$$V_L \in [(1-\beta\%)V_{LR},\ (1+\beta\%)V_{LR}] \quad (11)$$

where V_{LR} denotes the rated voltage of V_L and $\beta\%$ is the possible variable range of V_L.

Additionally, the input voltage of BIC, V_H, should be restrained within a specific range, especially with constant power load [31].

2) V_H cannot be too low as it must ensure BIC can maintain ac bus voltage.
3) V_H cannot be too high as large V_H brings large voltage stress on BIC.

Thus, the actual variable range of V_H is defined as

$$V_H \in [(1-\alpha\%)V_{HR}, (1+\alpha\%)V_{HR}] \quad (12)$$

where V_{HR} denotes the rated voltage of V_H and $\alpha\%$ is the possible variable range of V_H.

Since the ACLLC-type DCT must guarantee the well operation of BIC, the VCG of ACLLC-type DCT from LV side to HV side should be appropriately designed to meet this requirement. For convenience of description, the VCG of ACLLC-type DCT at LV → HV, defined as *M*, is derived as

$$M(\omega_{*1}, Q_1, g, k)|_{\mathrm{LV}\to\mathrm{HV}} = ||v_{\mathrm{C1D1}}/v_{\mathrm{AB}}|| = V_H/(nV_L) \triangleq \frac{k}{\sqrt{\lambda_3(\omega_{*1},Q_1,g)k^2 + \lambda_2(\omega_{*1},Q_1,g)k + \lambda_1(\omega_{*1},Q_1,g)}} \quad (13)$$

where

$$\lambda_{1L}(\omega_{*1},Q_1,g) = \frac{(\omega_{*1}^2-1)^2}{\omega_{*1}^4} \times \left[\frac{Q_1^2(g\omega_{*1}^2-1)^2}{g^2\omega_{*1}^2} + 1\right] \quad (>0) \quad (14a)$$

$$\lambda_{2L}(\omega_{*1},Q_1,g) = \frac{2(\omega_{*1}^2-1)}{\omega_{*1}^2} \times \left[\frac{Q_1^2(2g\omega_{*1}^2-g-1)(g\omega_{*1}^2-1)}{g^2\omega_{*1}^2} + 1\right] \quad (14b)$$

$$\lambda_{3L}(\omega_{*1},Q_1,g) = \frac{Q_1^2(2g\omega_{*1}^2-g-1)^2}{g^2\omega_{*1}^2} + 1 \quad (>1). \quad (14c)$$

Since the ACLLC-type DCT must ensure the well operation of BIC, the parameters should be appropriately designed to make VCG with LV → HV satisfy:

$$M \in \left[\, M_{\min},\, M_{\max} \,\right] \quad (15)$$

where

$$M_{\min} = (1-\alpha\%)\cdot V_{HR}/[n\cdot(1+\beta\%)\cdot V_{LR}] \quad (16a)$$

$$M_{\max} = (1+\alpha\%)\cdot V_{HR}/[n\cdot(1-\beta\%)\cdot V_{LR}]. \quad (16b)$$

Based on (15), it can be summarized from VCG point of view that *M* must guarantee (15) at any operation cases of ACLLC-type DCT in renewable energy system.

2) Design Criterion From VCG Point of View: To optimize the VCG, the intermediate parameters $\omega_{*1},\ Q_1,\ g$, and k must satisfy

$$(\omega_{*1}, Q_1, g, k) = \arg\min |M - M_R| \quad (17)$$

where M_R denotes the desired value of $M(\omega_{*1}, Q_1, g, k)$.

Equation (17) means the parameters $\omega_{*1},\ Q_1,\ g$, and k should minimize the value of $|M(\omega_{*1},\ Q_1,\ g,\ k) - M_R|$.

C. Further Simplification of the Above Criteria

According to (10) and (17), it can be observed that the criteria depend on four unknown parameters ω_{*1}, Q_1, g, and k, which interact with each other and are hardly achieved by only two known requirements in (4) and (15). Therefore, the design criteria are further simplified in this section.

1) Variable Range of ω_{*1}, Q_1, g, and k: For ω_{*1}: According to (2), (3a), and (9), the actual ω_{*1} varies in the following range:

$$\omega_{*1} \in \left[\omega_{*1\min}, \omega_{*1\max}\right] \tag{18a}$$

$$\omega_{*1\min} = \sqrt{(1-\zeta\%)(1-\xi\%)} f_{\omega_r}(k,g) \triangleq f_{\omega_{*1\min}}(k,g) \tag{18b}$$

$$\omega_{*1\max} = \sqrt{(1+\zeta\%)(1+\xi\%)} f_{\omega_r}(k,g) \triangleq f_{\omega_{*1\max}}(k,g) \tag{18c}$$

where $f\omega_r(k,g)$ refers to (9b); ζ and ξ are determined by the selected resonant components.

Thus, the range of ω_{*1} depends on the value of k and g. This is achieved from PT point of view to restrain the relationship between f_s and f_r.

For Q_1: To satisfy (15), it can be obtained that

$$M \le M_{\max} \Rightarrow F_1(k) \triangleq (\lambda_3 - 1/M_{\max}^2)k^2 + \lambda_2 k + \lambda_1 \ge 0 \tag{19a}$$

$$M \ge M_{\min} \Rightarrow F_2(k) \triangleq (\lambda_3 - 1/M_{\min}^2)k^2 + \lambda_2 k + \lambda_1 \le 0. \tag{19b}$$

To make (19) hold, the following condition should be satisfied [25]:

$$1 \le \lambda_3 \le \frac{1}{M_{\min}^2}, \text{ when } \begin{cases} Q_1 \in [0, \quad Q_{1\max}] \\ \omega_{*1} \in [\omega_{*1\min}, \quad \omega_{*1\max}]. \end{cases} \tag{20}$$

Substituting (14c) into (20), it can be derived that

$$0 < Q_1 \le Q_{1\max} \text{ when } \omega_{*1} \in \left[\omega_{*1\min}, \omega_{*1\max}\right] \tag{21a}$$

$$\begin{aligned} Q_{1\max} &= \frac{g\omega_{*1}}{M_{\min}} \sqrt{\frac{1-M_{\min}^2}{|2g\omega_{*1}^2 - g - 1|}} \\ &= \frac{\sqrt{1-[(1-\alpha\%)/(1+\beta\%)]^2} \cdot g\omega_{*1}}{[(1-\alpha\%)/(1+\beta\%)] \cdot |2g\omega_{*1}^2 - g - 1|} \\ &\triangleq f_{Q1\max}(k,g) \end{aligned} \tag{21b}$$

where α and β are determined by the specification of the predesigned actual renewable energy system. Therefore, $Q_{1\max}$ is also the function of k and g.

From (21), the range of Q_1 depends on the value of k and g.

For g: According to (2b) and (3d), the actual value of g is achieved

$$g = n^2 C_{r2R}/C_{r1R}. \tag{22}$$

Since the resonant capacitors are recommended to select the same material, C_{r1R} and C_{r2R} are changing with the same features. Therefore, the value of g basically remains the same at any power/temperature conditions.

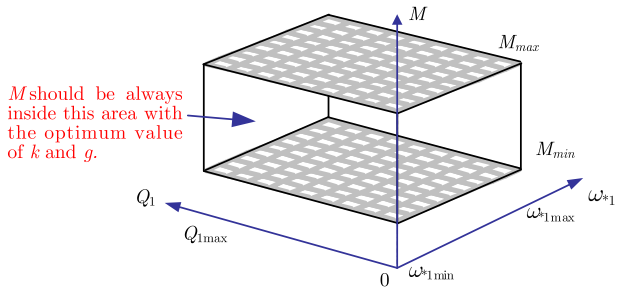

Fig. 4. Design criteria schematic of the ACLLC-type DCT.

For k: According to (2a) and (3e), the actual k is

$$k = L_{m1R}/L_{r1R} = L_{m2R}/L_{r2R}. \tag{23}$$

It is worth explaining that L_{m1} (L_{m2}) and L_{r1} (L_{r2}) denote the magnetizing inductance and leakage inductance of ACLLC-HFT, respectively, and they share the same magnetic core. Therefore, the value of k is relatively stable within allowable temperature [19].

Therefore, four unknown parameters ω_{*1}, Q_1, g, and k are transformed to two unknown parameters g and k, which are beneficial to simplify the parameter design.

2) Simplified Design Criteria: $\omega_{*1} \in |\omega_{*1\min}, \omega_{*1\max}|$ is utilized to ensure the PT. Meanwhile, M is function of (ω_{*1}, Q_1, g, k), and the ranges of Q_1 and ω_{*1} are determined by k and g. Therefore, the design criteria are summarized as follows: confirm the optimum k and g to make (24) hold (see Fig. 4)

$$M(k,g) \in [M_{\min}, \quad M_{\max}] \text{ when } \begin{cases} Q_1 \in \left[0, Q_{1\max}\right] \\ \omega_{*1} \in \left[\omega_{*1\min}, \omega_{*1\max}\right] \end{cases} \tag{24a}$$

$$(k,g) = \arg\min |M(k,g) - M_R| \tag{24b}$$

where $Q_1 \in [0, Q_{1\max}]$ mainly depends on the transmitted power, and $\omega_{*1} \in |\omega_{*1\min}, \omega_{*1\max}|$ is induced by the variation of the inductances and capacitances.

Remark I: The four unknown intermediate parameters ω_{*1}, Q_1, g, and k are transformed to only two parameters k and g, which avoids the needless calculations and greatly facilitates the parameter design. Besides, the proposed criteria in (24) are utilized to assist the VCG optimization on the premise of satisfied PT ability.

IV. Proposed Semi-AI Circuit Parameter Design

In this section, based on the design criteria in (24), a semi-AI circuit parameter design approach is proposed to derive the parameters L_{r1}, L_{r2}, L_{m1}, L_{m2}, C_{r1}, and C_{r2} of the ACLLC-type DCT at the rated temperature and power condition. It aims to realize the following:

1) Equation (24a) is satisfied to find the feasible solutions of k and g under the satisfactory PT ability.
2) Equation (24b) is to determine the optimum solution of k and g by optimizing the VCG.

The details are elaborated in the following.

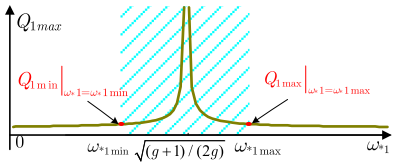

Fig. 5. $Q_{1\max}$ versus ω_{*1} curve.

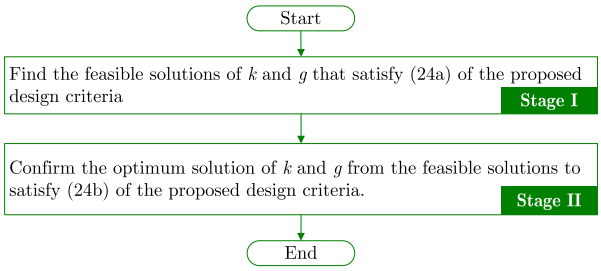

Fig. 6. Two-stage computer-assisted procedure of the proposed semi-AI design method.

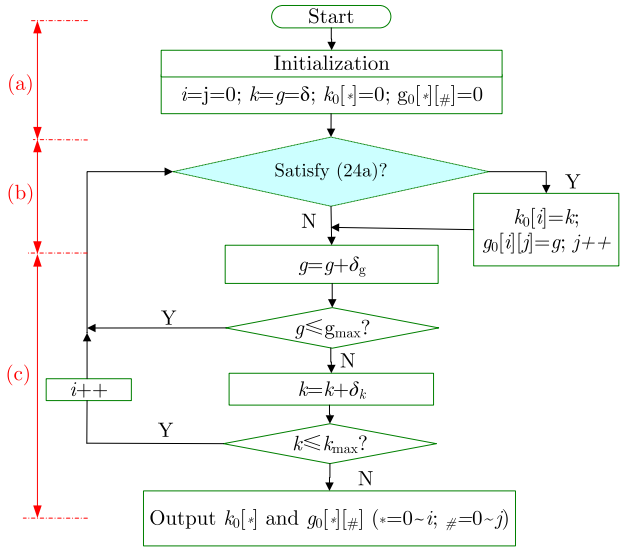

Fig. 7. Flowchart to find feasible solutions of k and g.

A. Preliminary of the Proposed Semi-AI Design Method

Before implementing the proposed semi-AI circuit parameter design, certain parameters are designed.

1) Design of n: To operate with the simple open loop, the turn ratio is selected as

$$n = V_{HR}/V_{LR}. \tag{25}$$

2) Design of ω_{rR}: According to (10), the theoretical resonant angular frequency at the rated power/temperature is

$$\omega_{rR} = 2\pi f_s. \tag{26}$$

3) Design of Q_{1R}: Q_{1R} denotes the maximum value of Q_1 at the rated power/temperature. According to (21b), Fig. 5 depicts $Q_{1\max}$ versus ω_{*1}. According to Fig. 5, it is obtained that

$$Q_{1R} = \min\left[Q_{1\max}|_{\omega_*1=\omega_*1\min}, Q_{1\max}|_{\omega_*1=\omega_*1\max}\right]. \tag{27}$$

B. Proposed Semi-AI Design Method

A two-stage computer-assisted procedure is introduced for the proposed semi-AI design method, as depicted in Fig. 6. Stage I is utilized to find the feasible solutions of k and g that satisfy (24a) of the proposed design criteria. Based on these feasible solutions, the optimum solution of k and g is determined to satisfy (24b) of the proposed design criteria in Stage II.

1) Stage I: Achieve the Feasible Solutions of k and g: To find the feasible solutions of k and g, a general approach shown in Fig. 7 is proposed. The details are elaborated as follows.

a) Initialization: $i, j, k_0[*]$, and $g_0[*][\#]$ are introduced to help store the feasible solutions of k and g that satisfy (24a). δ denotes the initial value of k and g, which is a small positive constant.

b) Find the feasible solutions of k and g: Equation (24a) in the proposed criteria must be satisfied to meet the VCG requirement, when the PT ability is guaranteed in the entire power range, i.e., $M(k, g) \in [M_{\min}, M_{\max}]$ when $Q_1 \in [0, Q_{1\max}]$ and $\omega_{*1} \in [\omega_{*1\min}, \omega_{*1\max}]$.

c) Update the values of k and g: According to (3d), since $g = n^2 C_{r2}/C_{r1}$, $g \to 0$ when $C_{r1} \to \infty$, and $g \to \infty$ when $C_{r2} \to \infty$. Therefore, the value of g varies within $(0, \infty)$. Here, $g_{\max}$ is recommended to be selected as 10^5 to simulate ∞. According to (3e), a larger value of k indicates a larger size of ACLLC-type HFT. As a result, though the maximal value of k can also be theoretically selected as $k_{\max} = \infty$, $k_{\max}$ is recommended to be selected with consideration of the actual volume and voltage gain requirements of the HFT. δ_k and δ_g denote the increment of k and g, respectively, which are determined by processor ability.

It can be observed from this procedure that each feasible solution of k can cooperate with more than one feasible solution of g. This also means that when the transformer is designed based on the feasible k, there are many choices of the capacitance ratio g to satisfy the VCG requirement.

2) Stage II: Determine the Optimum Solution of k and g: It is worthy to point out that the feasible solutions of k and g hardly maintain the deviation between M and M_R minimum. To solve this problem, the optimum solution of k and g is further confirmed by the approach shown in Fig. 8. The details are analyzed in the following.

a) Initialization: k_{opt} and g_{opt} are introduced to store the optimum solution of k and g, respectively. M_{error} is utilized to achieve the minimum value of the objective function.

b) Determine the optimum solution of k and g: To decrease computational burden, (24b) in the proposed criteria is converted into the following form:

$$f_{\text{obj}}(k, g) = \sum_{Q_1=0}^{Q1=Q_{1\max}} \sum_{\omega_{*1}=\omega_{*1}\min}^{\omega_{*1}=\omega_{*1}\min} |M - M_R|$$
$$\text{when} \begin{cases} k \in k[*] \\ g \in g_0[*][\#] \end{cases} \quad (* = 0 - i;\ \# = 0 - j). \tag{28}$$

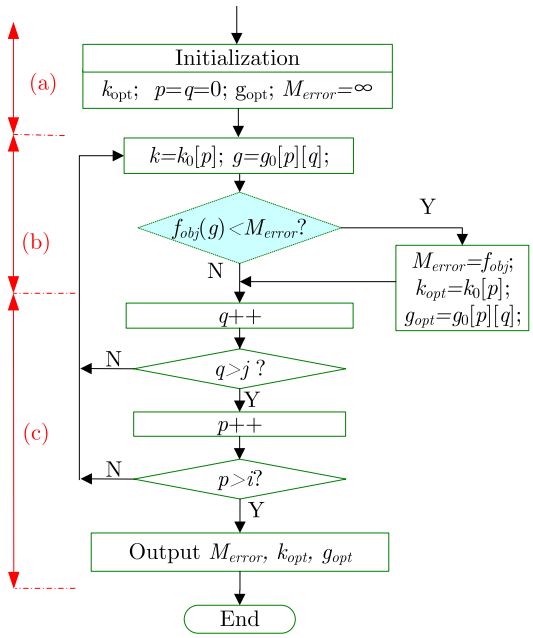

Fig. 8. Flowchart to achieve the optimum k and g of the ACLLC-type DCT.

TABLE I
SPECIFICATION OF THE ACLLC-TYPE DCT FOR VALIDATION

Parameters	Description	Value
V_L	LV side voltage	380 V
V_H	HV side voltage	760 V
f_s	Switching frequency	100 kHz
ζ% =ξ%	Variation of the resonant parameters	4%
α%=β%	Variation of the HV and LV side voltages	2%
P	Rated power	6 kW

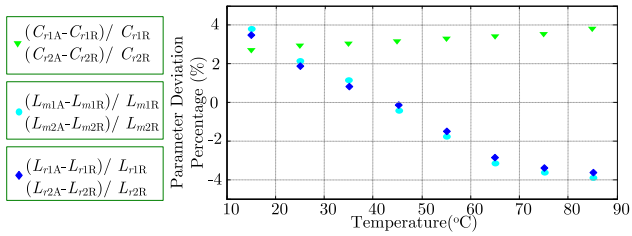

Fig. 9. Parameter deviation percentage under different temperatures.

c) Update the value of k and g: By substituting all feasible solutions of k and g into (28), the pair of k and g that makes $f_{\rm obj}(k, g)$ minimum can be finally accepted as optimum and stored in $k_{\rm opt}$ and $g_{\rm opt}$. This step is also illustrated in Fig. 8.

C. Determine the Parameters L_{r1R}, L_{r2R}, L_{m1R}, L_{m2R}, C_{r1R}, C_{r2R}

$$L_{r1R} = Q_{1R}R_H f_{\omega_r}(k_{\rm opt}, g_{\rm opt})/\omega_{rR} \tag{29a}$$
$$L_{r2R} = n^2 Q_{1R}R_H f_{\omega_r}(k_{\rm opt}, g_{\rm opt})/\omega_{rR} \tag{29b}$$
$$L_{m1R} = k_{\rm opt}Q_{1R}R_H f_{\omega_r}(k_{\rm opt}, g_{\rm opt})/\omega_{rR} \tag{29c}$$
$$L_{m2} = k_{\rm opt}n^2 Q_{1R}R_H f_{\omega_r}(k_{\rm opt}, g_{\rm opt})/\omega_{rR} \tag{29d}$$
$$C_{r1R} = f_{\omega_r}(k_{\rm opt}, g_{\rm opt})/Q_{1R}R_H\omega_{rR} \tag{29e}$$
$$C_{r2R} = g_{\rm opt}C_{r1R}/n^2. \tag{29f}$$

Remark II: Different from the conventional parameter design approach based on the complex derivations [19], [25], our proposed semi-AI optimal parameter design approach can be easily implemented via a simple looping algorithm. Besides, to offset the parameter variations in the full power range, the resonant parameters are determined via optimizing the VCG on the premise of the satisfied PT. Therefore, no closed-loop control is required as the PT and VCG can be naturally guaranteed with the proposed approach.

V. DESIGN EXAMPLE BASED ON THE PROPOSED SEMI-AI APPROACH

In this section, a detailed ACLLC-type DCT with the specifications shown in Table I is designed based on the proposed semi-AI design method. Note that the following procedures are only example to make the implementation of the proposed semi-AI design more accessible. The variation $\zeta\% = \xi\% = 4\%$ in Table I is achieved by measuring parameter deviation percentages within possible temperatures offline, as shown in Fig. 9. It is also noteworthy that if resonant components are made of various materials, structures, and so on, the variation 4% may be different.

A. Step-by-Step Parameter Determination

According to Section IV, step-by-step parameter design procedures of ACLLC-type DCT are elaborated as follows:

Step 1: Based on (25), $n = 2$; therefore, $M_R = 1$ can be achieved.
Step 2: According to (26), $\omega_{rR} = 628 \times 10^3$ rad/s.
Step 3: According to Section IV-B, considering the volume limitation and $f_{obj}(k, g)$, the optimum solution of k and g is achieved as

$$k_{\rm opt} = 50, \qquad g_{\rm opt} = 1.19. \tag{30}$$

Step 4: According to (21b), (27), and the values of $k_{\rm opt}$ and $g_{\rm opt}$ in Step 3, $Q_{1R} = 1.72$.
Step 5: According to (29) and the obtained n, ω_{rR}, Q_{1R}, $k_{\rm opt}$, and $g_{\rm opt}$, the values of the L_{r1R}, L_{r2R}, L_{m1R}, L_{m2R}, C_{r1R}, and C_{r2R} are derived as follows:

1) $L_{r1R} = 51.6\,\mu$H; $L_{m1R} = 2.58$ mH; $C_{r1R} = 0.0457\,\mu$F.
2) $L_{r2R} = 206.4\,\mu$H; $L_{m2R} = 10.32$ mH; $C_{r2R} = 0.0136\,\mu$F.

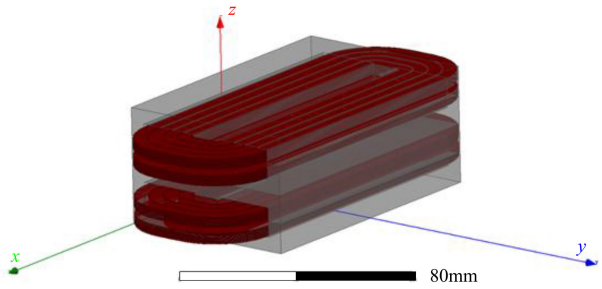

Fig. 10. 3-D model of the designed planar transformer.

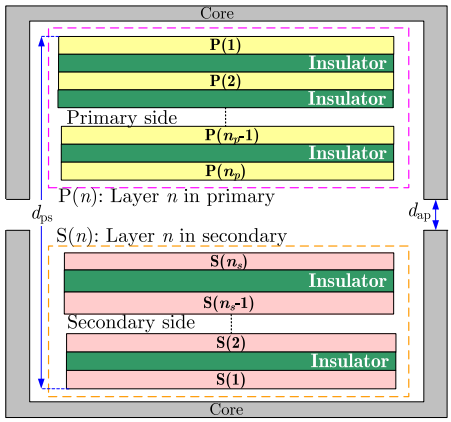

Fig. 11. Simplified diagram of the planar transformer.

B. Transformer Design Based on the Required Parameters in Step 5

1) Transformer Structure Selection: To achieve the optimum transformer parameters of Step 5, a high-frequency planar transformer is introduced in ACLLC-type DCT due to its advantages of excellent thermal characteristics, low profile, predictable parasitic parameters, etc. The magnetizing inductances are adjusted by the number of the turns and the air gap, while the leakage inductances are regulated by the distance between primary and secondary windings.

In order to acquire the desired resonant leakage inductance as well as the magnetizing inductance at the rated power, four ferrite magnetic cores are employed with the same type ELP64 (width)/10 (depth)/50 (length) to make the design procedure flexible. By means of the ANSYS Maxwell, the established three-dimensional (3-D) model of the transformer is shown in Fig. 10, with the details illustrated in the following.

2) Transformer Design to Achieve the Required Resonant Parameters: The simplified diagram of the planar transformer is shown in Fig. 11, where d_{ps} indicates the total thickness of the windings, d_{ap} is the thickness of the air gap, and n_p and n_s are primary and secondary winding numbers, respectively. Since the required parameters in Step 5 depend on n_p, n_s, d_{ps}, and d_{ap}, two procedures are conducted in the following.

a) Procedure I: Obtain n_p, n_s, and d_{ps} based on required L_{r1R}: The specific procedure I is rearranged in Fig. 12(a), where

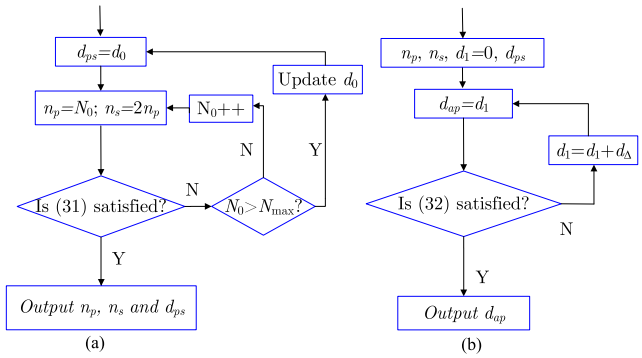

Fig. 12. Flowchart to achieve (a) n_p, n_s, and d_{sp}, and (b) d_{ap}.

$N_{\max}$ depends on the area of transformer window, and d_0 and N_0 are utilized to update the value of d_{ps} and n_p, respectively. Since L_{r1} is proportional to n_p and d_{ps} [33], and the larger value of n_p brings more copper loss, d_0 is initially set large enough in the permitted range, and N_0 is initially set small enough.

In Fig. 12(a), by calculating the value of L_{r1} with the magnetic energy method in [34], the values of n_p, n_s, and d_{ps} will be output once the value of L_{r1} satisfies

$$(1-\zeta\%)L_{r1R} \le L_{r1} \le (1+\zeta\%)L_{r1R} \tag{31}$$

otherwise, the values of d_0 and N_0 will be updated in the allowable range.

Therefore, combining the parameters $N_{\max} = 50$, $d_0 = 9.5$ mm, and the given L_{r1R}, it can be finally achieved that $n_p = 30$, $n_s = 60$, and $d_{ps} = 9.75$ mm.

b) Procedure II: Acquire d_{ap} based on the obtained L_{m1R}: Fig. 12(b) shows the flowchart to determine d_{ap}, whose initial value is set as zero. By means of the magnetic circuit analysis in [35], L_{m1} can be derived with the known n_p, n_s, and d_{ps}. The value of d_{ap} will be confirmed, if L_{m1} satisfies

$$(1-\zeta\%)L_{m1R} \le L_{m1} \le (1+\zeta\%)L_{m1R} \tag{32}$$

otherwise, the value of d_1 will be updated with the fixed interval d_Δ.

Combining the parameters in Procedure I and the given L_{m1R}, $d_{ap} = 0.57$ mm is finally confirmed.

3) Designed Transformer Verification: To verify the correctness of the values n_p, n_s, d_{ps}, and d_{ap}, the finite-element analysis simulation has been conducted with the help of ANSYS Maxwell. The distributions of magnetic flux density @ 100 kHz for the leakage and magnetic inductances are achieved in Fig. 13. Table II summarizes the simulated and target values of $L_{r1(2)R}$ and $L_{m1(2)R}$. It can be concluded from Table II that the simulated value shows acceptable relative error, which validates the successful transformer design.

To make the proposed semi-AI approach more accessible, a flowchart has been summarized in Fig. 14. Note that all resonant parameter variations have been considered to reduce the unknown parameter number. As a result, the simplified criteria in (24) can be derived to guide the semi-AI design. Besides, the transformer design in Section V is just an implementation

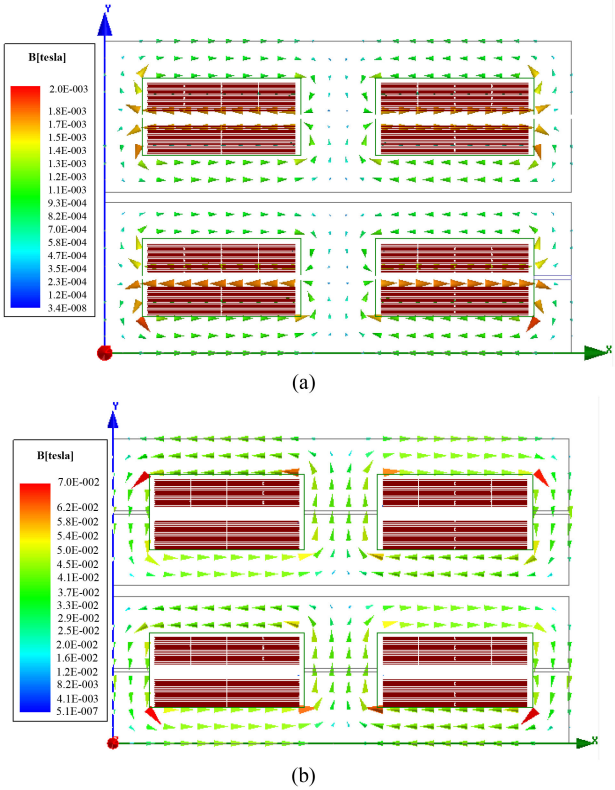

Fig. 13. Distribution of magnetic flux density @ 100 kHz for (a) leakage inductance and (b) magnetizing inductance.

TABLE II
COMPARISON BETWEEN SIMULATED AND TARGET RESONANT PARAMETERS

Parameters	Simulated value	Target value	Relative error (%)
L_{r1R}	52.6 μH	51.6 μH	1.94
L_{r2R}	210.4 μH	206.4 μH	1.94
L_{m1R}	2.58 mH	2.58 mH	0
L_{m2R}	10.32mH	10.328mH	0

method to obtain the acquired resonant parameters. If the power density should be further improved, not only the special transformer design should be considered, but also the proper structure design, efficient PCB design, and cooling way are essential. These are vital to optimize the power density, but not the focus of this paper; thus, the power density improvement will be studied in future.

VI. EXPERIMENTAL VERIFICATION

Based on the design example of Section V, an ACLLC-type DCT prototype is developed and integrated into a real renewable energy system as given in Fig. 15. The dc programmable source is utilized to simulate PV. Both the dc and ac load banks are introduced to obtain various load profiles. The BIC directly tied with HV side of DCT is employed to construct ac subgrid. The battery energy storage system is introduced to establish dc subgrid, which is also tied to the LV side of DCT. AC output of

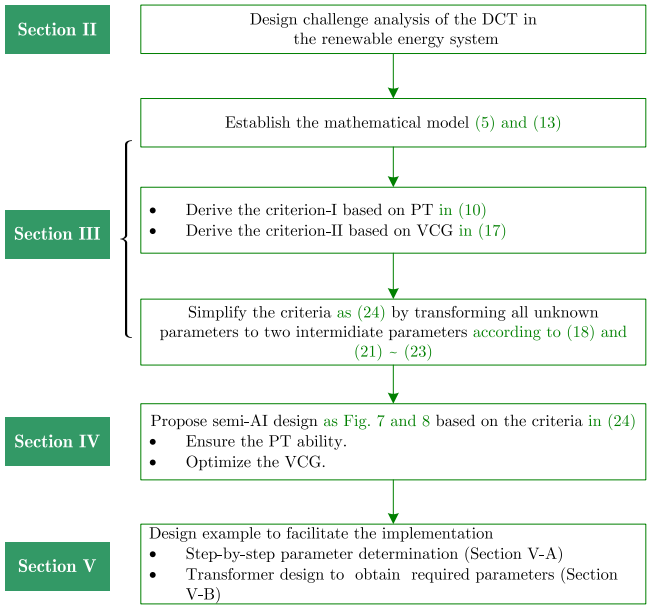

Fig. 14. Flowchart of the proposed semi-AI approach.

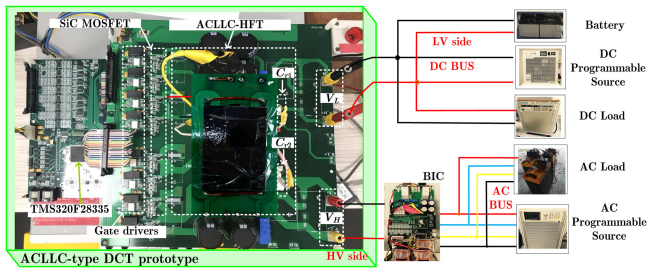

Fig. 15. ACLLC-type DCT based on renewable energy system prototype.

TABLE III
PRACTICAL SPECIFICATIONS OF ACLLC-TYPE DCT

Item		Parameter
Semiconductor device		C2M0080120D
Resonant capacitor		940C30SXK-F(X=1/15/22)
C_{r1}		0.0457 μF
C_{r2}		0.0136 μF
Digital signal processor		TMS320F28335
Switching dead-time		100 ns
Transformer	Core material	Ferrite
	Primary windings	30 turns
	Secondary windings	60 turns
Number of SiC-MOSFET		8
Output Capacitance of SiC-MOSFET (C_{oss})		80 pF
Drain-source on-state resistance		80 mΩ

BIC is directly connected with ac programmable source, which simulates the utility grid. BIC is regulated by the DSPACE.

The detailed experimental parameters of the ACLLC-type DCT are described in Table III and Section V. Since the designed parameters are robust enough against the variations of the temperature and power, the DSP board is only utilized to

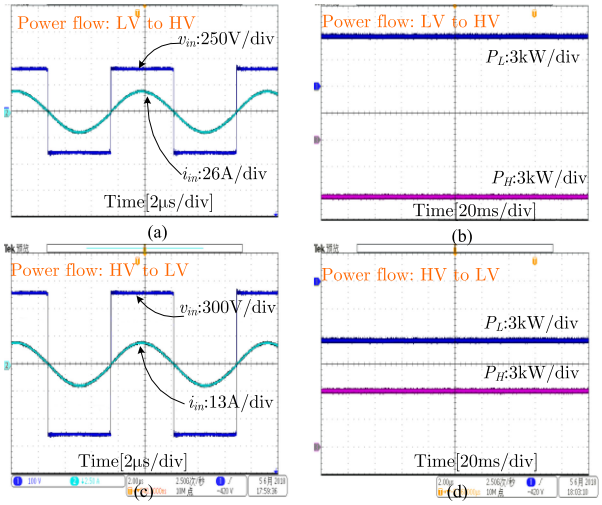

Fig. 16. Waveforms of ACLLC-type DCT at rated power. (a) Voltage and current waveforms with power transmitted as LV → HV. (b) Power waveforms with power transmitted as LV → HV. (c) Voltage and current waveforms with power transmitted as HV → LV. (d) Power waveforms with power transmitted as HV → LV.

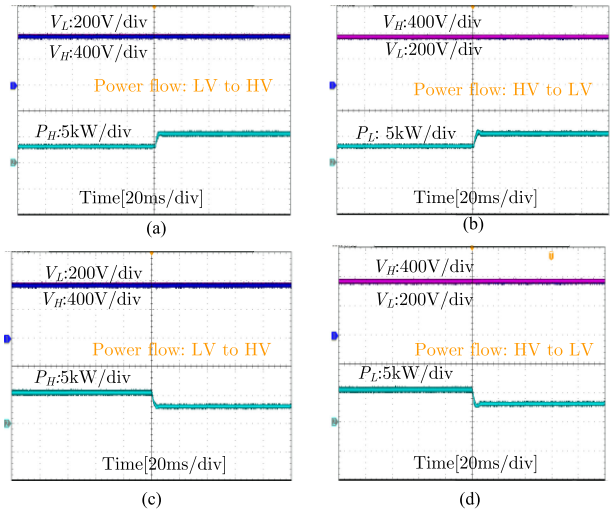

Fig. 17. Waveforms of the voltages and power of ACLLC-type DCT under $f_s = f_r$. The power is transmitted with (a) LV → HV and (b) HV → LV from half to full load. The power is transmitted with (c) LV → HV and (d) HV → LV from full to half load.

provide the pulse with fixed frequency. Therefore, no feedback is required in the designed DCT system.

A. Bidirectional Power Flow Characteristics

The characteristics of ACLLC-type DCT are tested in this section to verify the effectiveness of the designed transformer and resonant network. When $f_s = f_r$, the results are depicted in Fig. 16, where v_{in} (i.e., v_{AB} in Fig. 16(a) and v_{CD} in Fig. 16(c)) and i_{in} (i.e., i_{AB} in Fig. 16(a) and i_{CD} in Fig. 16(c)) indicate the equivalent input voltage and current of the ACLLC-HFT respectively.

As illustrated in Fig. 16(a), v_{in} and i_{in} are kept in phase to reduce the conduction loss when the rated power is transmitted with LV → HV, and Fig. 16(b) presents the corresponding power waveforms. When power is transmitted with HV → LV, the same ACLLC-type DCT characteristics are presented in Fig. 16(c) and (d).

B. PT and VCG Verification

As measured in Fig. 9, the practical values of the inductances and capacitances are changing with the temperature; thus, f_r varies online. Meanwhile, f_s is constant in the open-loop control. Therefore, the real f_s/f_r is not constant in practice. For the determined resonant parameters, it is hard to regulate f_s/f_r by changing f_r in the experiment. Fortunately, f_s can be easily changed online. Therefore, the variation of f_s/f_r can be experimentally simulated by slightly changing f_s online to verify the characteristics of the proposed method. Consequently, in this section, the parameter variations with $f_s/f_r \in [0.96, 1.04]$ given in Section V are introduced to simulate the temperature variation by changing f_s.

1) PT Characteristics: The PT ability against the parameter variations has been verified, as shown in Figs. 17 and 18.

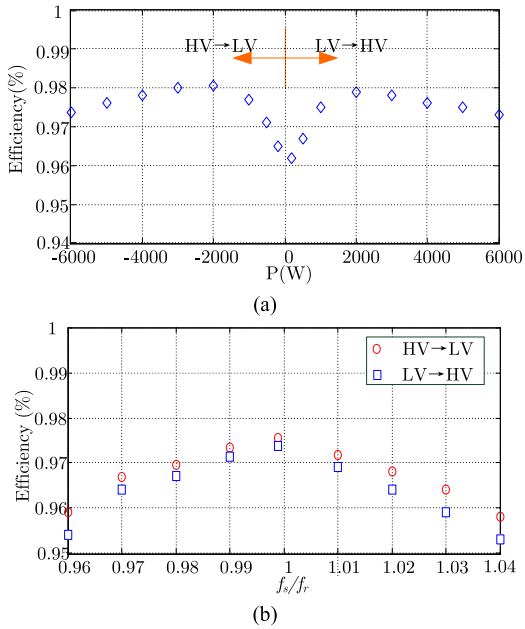

Fig. 18. Efficiency of ACLLC-type DCT (a) in entire power range when $f_s = f_r$ and (b) when f_s varies within $[0.96f_r, 1.04f_r]$ at rated power.

As observed from Fig. 17 with $f_s = f_r$, $2V_L$ is basically the same with V_H, no matter the power is changed from half to full load or from full to half load bidirectionally. Besides, the transient settling time is less than 6 ms under the bidirectional PT conditions to recover to the new steady status. The similar waveforms can be achieved by considering the parameter variations with $f_s/f_r \in [0.96, 1.04]$ when power varies between half and full load bidirectionally.

Practically, the efficiency of ACLLC-type DCT directly reflects its PT ability. Fig. 18 depicts the efficiency of ACLLC-type DCT when both power and f_s/f_r vary bidirectionally. Fig. 18(a) shows bidirectional efficiency of ACLLC-type DCT

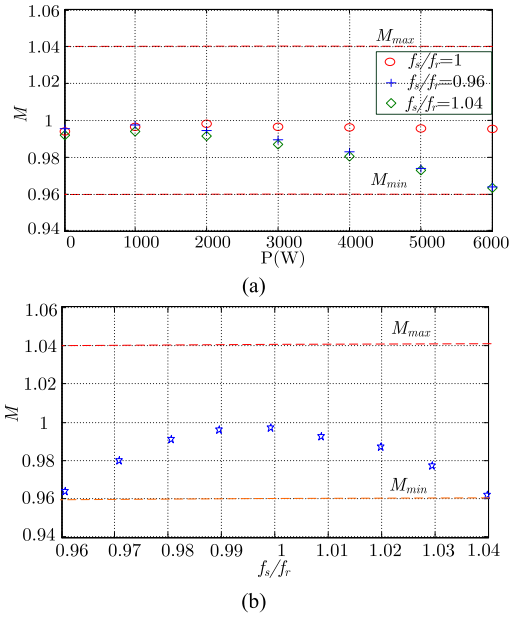

Fig. 19. M of ACLLC-type DCT at (a) entire power range and (b) rated power.

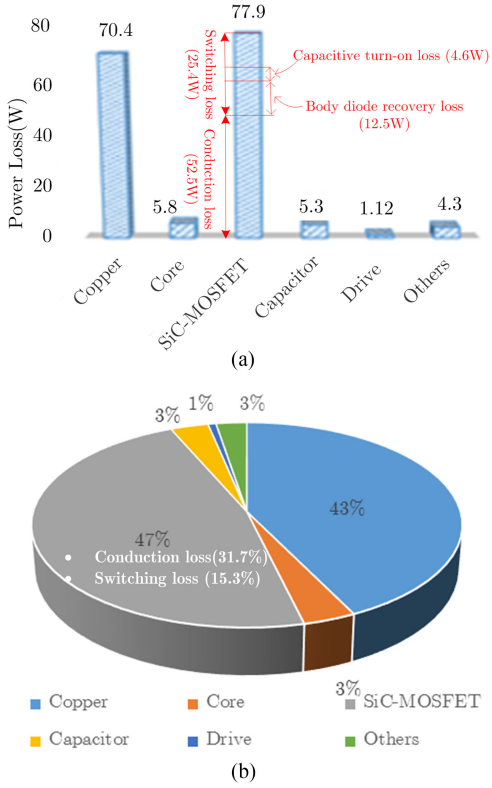

Fig. 20. System loss breakdown at rated power. (a) Power loss (W). (b) Power loss ratio.

at $f_s/f_r = 1$ in entire power range. The maximum efficiency is close to 98.2%. Fig. 18(b) depicts bidirectional efficiency of ACLLC-type DCT when f_s/f_r varies within [0.96, 1.04] at rated power condition.

These results verify the satisfactory PT ability of the designed ACLLC-type DCT while considering the parameter variations.

2) VCG Characteristics: In order to achieve VCG characteristics against parameter variations, M of the designed ACLLC-type DCT with LV $\rightarrow$ HV has been measured at entire power range, as summarized in Fig. 19.

Fig. 19(a) shows M of ACLLC-type DCT at entire power range when the value of f_s/f_r is selected as 0.96, 1, and 1.04. It can be observed that for the given f_s/f_r, M is decreased with power. Fig. 19(b) presents M of ACLLC-type DCT at rated power when f_s/f_r is changed from 0.96 to 1.04. The ACLLC-type DCT can always keep its M between $M_{\min}$ (0.96) and $M_{\max}$ (1.04), which satisfies the VCG requirement in (15). Thus, the designed ACLLC-type DCT enjoys robust VCG.

C. Other Characteristics of the Proposed DCT

1) Loss Analysis: The detailed system loss breakdown at the rated power is depicted in Fig. 20, where the loss of the power semiconductor device (SiC MOSFET) involves the conduction and switching losses. Fig. 20(a) presents the specific power loss value, and Fig. 20(b) summarizes the power loss ratio. It is noteworthy that both the capacitive turn-ON loss and the body diode recovery loss are considered to derive the switching loss. It can be observed that the loss is mainly induced by the SiC MOSFET and the copper of transformer. Since the copper loss largely depends on the power rating and the winding configuration of the transformer, it is not the focus of this paper. Meanwhile, the conduction loss of the SiC MOSFET largely depends on the device itself. Therefore, only the switching loss of the SiC MOSFET will be further discussed in the following.

In the proposed approach, both the good PT and optimum VCG are conductive to reduce the switching loss by keeping high power factor and quasi-zero current switching. To verify this, the device voltage, current, and driver voltage of SiC MOSFET have been measured in the full power range, as shown in Fig. 21. Apparently, by adopting the proposed approach, the semiconductor device (SiC MOSFET) is turned ON and OFF only when the resonant current is basically zero. Therefore, the switching loss of the device is small in the entire power range. These results are consistent with Remark II.

2) Characteristics of the Proposed DCT Under Various Input Voltages: To verify the characteristics of the proposed DCT under various input voltages, the output dc voltage, power, and HFT input voltage and current are given in Fig. 22 when the transmitted power remains unchanged.

It can be observed that under different input dc voltages (LV side) of 300 V in Fig. 22(a) and 200 V in Fig. 22(b), the output dc voltage (HV side) is kept n (=2) times of the input voltage (LV side), which indicates that the robust VCG ability is guaranteed under various input voltages. In addition, the input voltage of HFT is kept in phase with its input current based on the enlarged part of Fig. 22, and thus the satisfactory PT ability is obtained.

3) HFT Current (i.e., Switch Current) Analysis Under Different Load Conditions: The HFT current is constituted by the

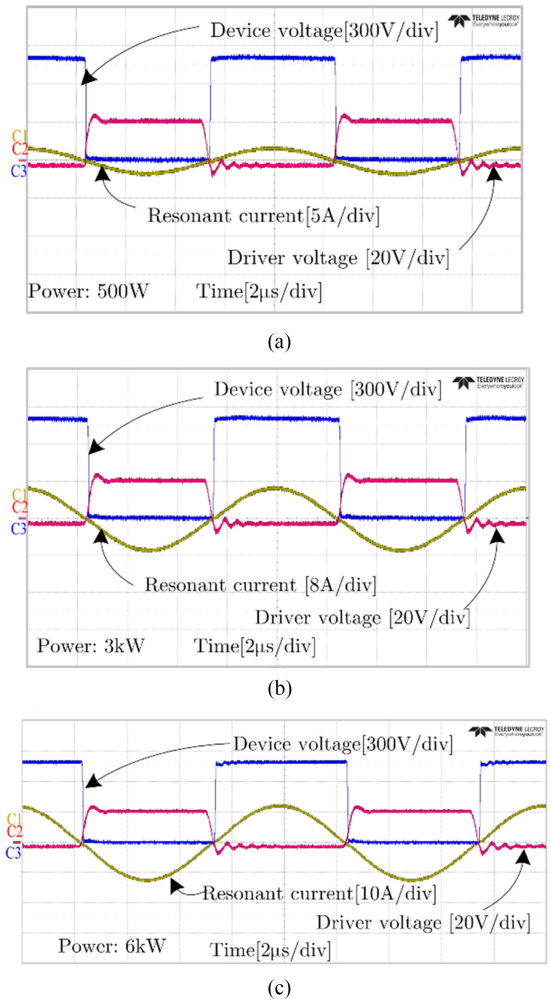

Fig. 21. Waveforms of the device voltage, driver voltage, and resonant current at different powers. (a) 500 W. (b) 3 kW. (c) 6 kW.

switch current of the upper arm at the positive half cycle, and switch current of the lower arm at the negative half cycle. Therefore, if the HFT current is measured, the switch currents of both the upper and lower arms will be obtained.

The HFT currents at both LV side and HV side have been tested at different load conditions, as shown in Fig. 23. Obviously, HFT current at LV side is kept sinusoidal and its value is n (=2) times of that at the HV side in entire power range.

These results also mean that the proposed approach effectively guarantees that the switch currents at both LV side and HV side change in synchronization in the entire power range and are maintained in the same phase with HFT voltage to reduce conduction loss.

4) Transient Characteristics of the Proposed DCT: The characteristics of the proposed DCT when the load transient occurs are further analyzed in this section. When the power reference is changed from 3 to 5 kW, the results are given in Fig. 24, where the actual power recovers to its new steady state within 1 ms. Meanwhile, the dc voltage at the LV side is kept stable during this transient.

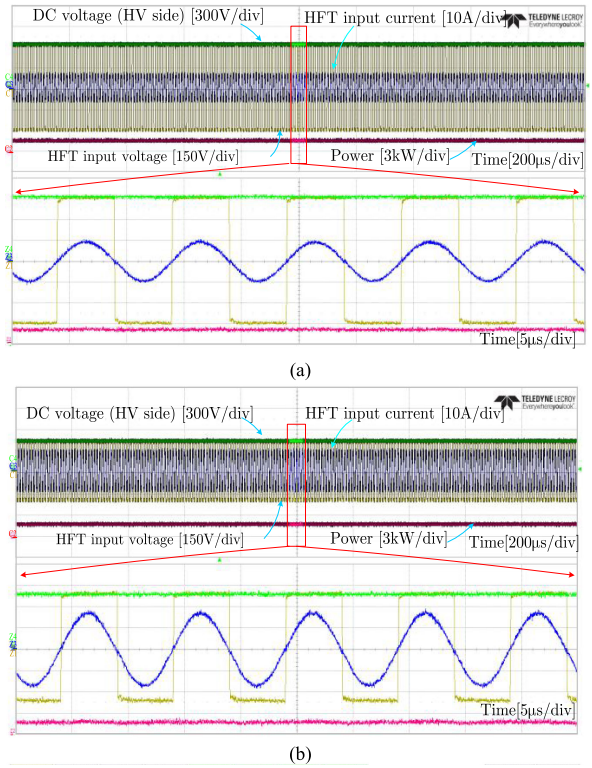

Fig. 22. Waveforms of output dc voltage (HV side), power, and HFT input voltage and current under different input dc voltages (LV side). (a) 300 V input dc voltage. (b) 200 V input dc voltage.

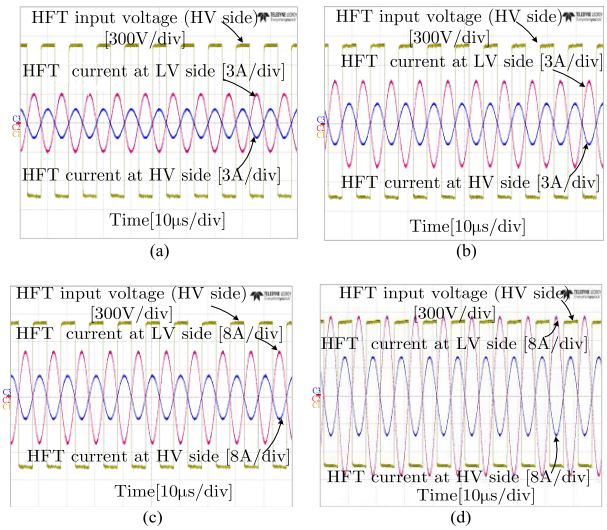

Fig. 23. Waveforms of the HFT currents and input voltage under different load conditions. (a) 500 W. (b) 700 W. (c) 3 kW. (d) 5.6 kW.

D. Comparison Between the Approach in [25] and the Proposed Approach

To demonstrate the superiority of the proposed approach, both the PT and VCG ability have been compared with the approach in [25]. For a fair comparison, the related resonant components adopt the same material.

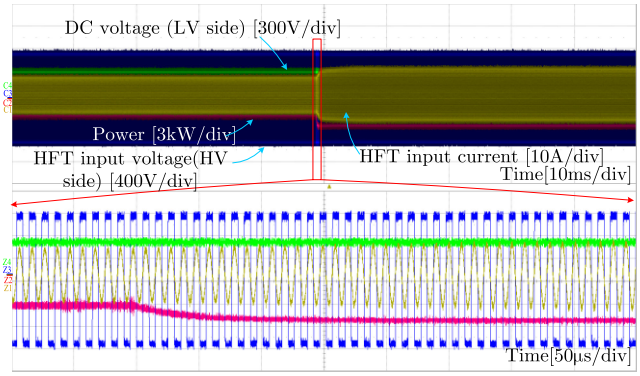

Fig. 24. Transient waveforms of designed DCT.

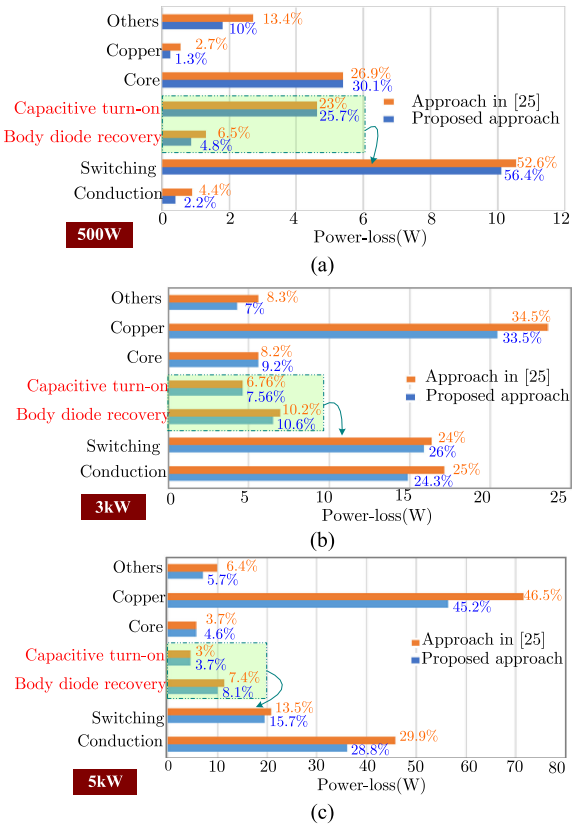

Fig. 25. Power loss breakdown comparison of the approach in [25] and the proposed approach at (a) 500 W, (b) 3 kW, and (c) 5 kW.

Since the superiority of PT ability can be evaluated by efficiency, the detailed power loss breakdown has been compared as shown in Fig. 25, where the capacitive turn-ON loss and the body diode recovery loss are taken in account to obtain the switching loss. During the light-load condition as Fig. 25(a), the power loss is mainly induced by the switching and core. When the power is further increased as shown in Fig. 25(b) and (c), it can be observed that compared to the approach in [25], the copper loss of the proposed approach is reduced by more than 13%, and its conduction loss is reduced by more than 10% because the proposed approach is beneficial to suppress the amplitude of the resonant current. Therefore, the proposed approach exhibits satisfactory efficiency as shown in Fig. 18.

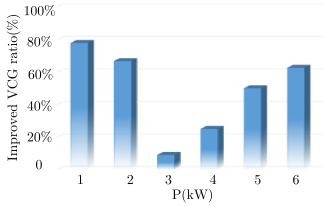

Fig. 26. Improved VCG ratio of the proposed approach in entire power range.

For the VCG ability comparison, the improved VCG ratio of the proposed approach is introduced by $(|M - M_R|_{[25]} - |M - M_R|_{\text{proposed approach}})/|M - M_R|_{[25]}$, where $|M - M_R|_{[25](\text{proposed approach})}$ is the value of $|M - M_R|$ obtained by [25] (the proposed approach). The results are shown in Fig. 26. Apparently, the maximum value of the improved VCG ratio is close to 80%, and the average value of the improved VCG ratio in Fig. 26 is more than 40%.

These comparisons further verify the superiority of VCG ability in the proposed approach.

VII. Conclusion

In the renewable energy system, the ACLLC-type DCT is usually recommended to employ the low-cost open-loop control to corporate with BIC to simplify the systematic design. However, this ACLLC-type DCT may lose its required VCG and deteriorate the PT ability of the renewable energy system when the resonant frequency changes in different operation cases. Therefore, a semi-AI-based circuit design method has been put forward in this paper, combining the advantages of both mathematical-model-based and AI-based design methods and removing their shortages. It replaces all unknown parameters with two intermediate parameters to optimally design the parameters of the circuit via a very simple computer-assisted procedure. With the proposed method, not only good PT ability is guaranteed, but also optimized VCG is achieved against the parameter variations. In addition, an example with a planar transformer design is further illustrated with the aid of ANSYS Maxwell. Finally, an experimental ACLLC-type DCT prototype has been embedded in a real renewable energy system to verify the effectiveness of the proposed design method. Based on the designed parameters, the optimum switching frequency should be further selected to ensure the high efficiency, which is recommended as a potential future work direction.

References

[1] A. Ajami, H. Ardi, and A. Farakhor, "A novel high step-up dc/dc converter based on integrating coupled inductor and switched-capacitor techniques for renewable energy applications," *IEEE Trans. Power Electron.*, vol. 30, no. 8, pp. 4255–4263, Aug. 2015.

[2] X. Zhang and Q. Zhong, "Improved adaptive-series-virtual-impedance control incorporating minimum ripple point tracking for load converters in dc systems," *IEEE Trans. Power Electron.*, vol. 31, no. 12, pp. 8088–8095, Dec. 2016.

[3] P. Wang, L. Goel, X. Liu, and F. H. Choo, "Harmonizing ac and dc: A hybrid ac/dc future grid solution," *IEEE Power Energy Mag.*, vol. 11, no. 3, pp. 76–83, May/Jun. 2013.

[4] X. Zhang, Q. Zhong, V. Kadirkamanathan, J. He, and J. Huang, "Source-side series-virtual-impedance control to improve the cascaded system stability and the dynamic performance of its source converter," *IEEE Trans. Power Electron.*, vol. 34, no. 6, pp. 5854–5866, Jun. 2019.

[5] T. Dragičević, X. Lu, J. C. Vasquez, and J. M. Guerrero, "DC microgrids—Part II: A review of power architectures, applications, and standardization issues," *IEEE Trans. Power Electron.*, vol. 31, no. 5, pp. 3528–3549, May 2016.

[6] M. H. Ryu, H. S. Kim, J. W. Baek, H. G. Kim, and J. H. Jung, "Effective test bed of 380-V dc distribution system using isolated power converters," *IEEE Trans. Ind. Electron.*, vol. 62, no. 7, pp. 4525–4536, Jul. 2015.

[7] B. Liu, X. Shi, Y. Li, F. F. Wang, and L. M. Tolbert, "A line impedance conditioner for saturation mitigation of zigzag transformer in hybrid ac/dc transmission system considering line unbalances," *IEEE Trans. Power Electron.*, vol. 32, no. 7, pp. 5070–5086, Jul. 2017.

[8] Y. Xia, W. Wei, M. Yu, Y. Peng, and J. Tang, "Decentralized multi-time scale power control for a hybrid ac/dc microgrid with multiple subgrids," *IEEE Trans. Power Electron.*, vol. 33, no. 5, pp. 4061–4072, May 2018.

[9] J. Huang and X. Zhang, "Three-step switching frequency selection criteria for symmetrical *CLLC*-type dc transformer in hybrid ac/dc microgrid," *IEEE Trans. Power Electron.*, vol. 34, no. 10, pp. 9379–9385, Oct. 2019.

[10] J. Xiao, X. Bac, J. Huang, and Q. Zhou, "Implementation of dc/dc converter with high frequency transformer (DHFT) in hybrid ac/dc microgrid," in *Proc. Asian Conf. Energy, Power Transp. Electrific. (ACEPT)*, 2017, pp. 1–5.

[11] S. Zhao, Q. Li, F. C. Lee, and B. Li, "High-frequency transformer design for modular power conversion from medium-voltage ac to 400 Vdc," *IEEE Trans. Power Electron.*, vol. 33, no. 9, pp. 7545–7557, Sep. 2018.

[12] L. Kong and H. Nian, "Collaborative control strategy of power electronic transformer and fault current limiter in dc microgrid," *J. Eng.*, vol. 2017, no. 13, pp. 1788–1792, 2017.

[13] Y. Zheng, S. Li, and R. Tan, "Distributed model predictive control for on-connected microgrid power management," *IEEE Trans. Control Syst. Technol.*, vol. 26, no. 3, pp. 1028–1039, May 2018.

[14] M. Davari and Y. A. R. I. Mohamed, "Robust multi-objective control of VSC-based dc-voltage power port in hybrid ac/dc multi-terminal micro-grids," *IEEE Trans. Smart Grid, vol.* 4*, no.* 3*, pp.* 1597–1612*,* Sep. 2013.

[15] S. Inoue and H. Akagi, "A bidirectional dc–dc converter for an energy storage system with galvanic isolation," *IEEE Trans. Power Electron.*, vol. 22, no. 6, pp. 2299–2306, Nov. 2007.

[16] B. Zhao, Q. Song, W. Liu, and Y. Sun, "Overview of dual-active-bridge isolated bidirectional dc–dc converter for high-frequency-link power-conversion system," *IEEE Trans. Power Electron.*, vol. 29, no. 8, pp. 4091–4106, Aug. 2014.

[17] C. H. Chang, E. C. Chang, and H. L. Cheng, "A high-efficiency solar array simulator implemented by an *LLC* resonant dc–dc converter," *IEEE Trans. Power Electron.*, vol. 28, no. 6, pp. 3039–3046, Jun. 2013.

[18] S. Fan, W. Ma, T. C. Lim, H. Chaoui, and M. Benghanem, "Design and control of a wind energy conversion system based on a resonant dc/dc converter," *IET Renewable Power Gener.*, vol. 7, no. 3, pp. 265–274, May 2013.

[19] J. H. Jung, H. S. Kim, M. H. Ryu, and J. W. Baek, "Design methodology of bidirectional *CLLC* resonant converter for high-frequency isolation of dc distribution systems," *IEEE Trans. Power Electron.*, vol. 28, no. 4, pp. 1741–1755, Apr. 2013.

[20] W. Chen, P. Rong, and Z. Y. Lu, "Snubberless bidirectional dc–dc converter with new *CLLC* resonant tank featuring minimized switching loss," *IEEE Trans. Ind. Electron.*, vol. 57, no. 9, pp. 3075–3086, Sep. 2010.

[21] J. Huang, J. Xiao, C. Wen, P. Wang, and A. Zhang, "Implementation of bidirectional resonant dc transformer in hybrid ac/dc micro-grid," *IEEE Trans. Smart Grid*, vol. 10, no. 2, pp. 1532–1542, Mar. 2019.

[22] L. Xue, Z. Shen, D. Boroyevich, P. Mattavelli, and D. Diaz, "Dual active bridge-based battery charger for plug-in hybrid electric vehicle with charging current containing low frequency ripple," *IEEE Trans. Power Electron.*, vol. 30, no. 12, pp. 7299–7307, Dec. 2015.

[23] Y. S. Lee and G. T. Cheng, "Quasi-resonant zero-current-switching bidirectional converter for battery equalization applications," *IEEE Trans. Power Electron.*, vol. 21, no. 5, pp. 1213–1224, Sep. 2006.

[24] X. Li and A. K. S. Bhat, "Analysis and design of high-frequency isolated dual-bridge series resonant dc/dc converter," *IEEE Trans. Power Electron.*, vol. 25, no. 4, pp. 850–862, Apr. 2010.

[25] J. Huang *et al.*, "Robust circuit parameters design for the *CLLC*-type dc transformer in the hybrid ac/dc microgrid," *IEEE Trans. Ind. Electron.*, vol. 66, no. 3, pp. 1906–1918, Mar. 2019.

[26] B. Zhao, X. Zhang, and J. Huang, "AI algorithm based two-stage optimal design methodology of high-efficiency *CLLC* resonant converters for the hybrid ac/dc microgrid applications," *IEEE Trans. Ind. Electron.*, vol. 66, no. 12, pp. 9756–9767, Dec. 2019.

[27] F. Nejabatkhah and Y. W. Li, "Overview of power management strategies of hybrid ac/dc microgrid," *IEEE Trans. Power Electron.*, vol. 32, no. 12, pp. 7072–7089, Dec. 2015.

[28] J. Huang, F. Guo, C. Wen, B. Yang, and J. Xiao, "A direct power control strategy for ac/dc converter based on best switching state approach," *IEEE J. Emerg. Sel. Top. Power Electron.*, vol. 6, no. 4, pp. 2273–2286, Dec. 2018.

[29] C. Carretero, J. Acero, R. Alonso, J. M. Burdio, and F. Monterde, "Temperature influence on equivalent impedance and efficiency of inductor systems for domestic induction heating appliances," in *Proc. 22nd Annu. IEEE Appl. Power Electron. Conf. Expo.*, 2007, pp. 1233–1239.

[30] X. Liu, P. C. Loh, P. Wang, and F. Blaabjerg, "A direct power conversion topology for grid integration of hybrid ac/dc energy resources," *IEEE Trans. Ind. Electron.*, vol. 60, no. 12, pp. 5696–5707, Dec. 2013.

[31] Q. Xu, C. Zhang, C. Wen, and P. Wang, "A novel composite nonlinear controller for stabilization of constant power load in dc microgrid," *IEEE Trans. Smart Grid*, vol. 10, no. 1, pp. 752–761, Jan. 2019.

[32] M. A. Saket, N. Shafiei, and M. Ordonez, "*LLC* converters with planar transformers: Issues and mitigation," *IEEE Trans. Power Electron.*, vol. 32, no. 6, pp. 4524–4542, Jun. 2017.

[33] J. Zhang, Z. Ouyang, M. C. Duffy, M. A. Andersen, and W. G. Hurley, "Leakage inductance calculation for planar transformers with a magnetic shunt," *IEEE Trans. Ind. Appl.*, vol. 50, no. 6, pp. 4107–4112, Nov./Dec. 2014.

[34] Z. Ouyang, J. Zhang, and W. G. Hurley, "Calculation of leakage inductance for high-frequency transformers," *IEEE Trans. Power Electron.*, vol. 30, no. 10, pp. 5769–5775, Oct. 2015.

[35] Z. Ouyang, O. C. Thomsen, and M. A. E. Andersen, "Optimal design and tradeoff analysis of planar transformer in high-power dc–dc converters," *IEEE Trans. Ind. Electron.*, vol. 59, no. 7, pp. 2800–2810, Jul. 2012.

Jingjing Huang (S'11–M'18) received the B.S. degree in electrical engineering from the Henan University of Science and Technology, Luoyang, China, in 2008, and the Ph.D. degree in electrical engineering from Xi'an Jiaotong University, Xi'an, China, in 2014.

Since April 2014, she has been a Lecturer with the Xi'an University of Technology, Xi'an, China. Since December 2016, she has been a Research Fellow with Nanyang Technological University, Singapore. She has authored or coauthored more than 60 technique papers. She holds more than ten patents. Her research interests include renewable energy systems, high-frequency transformers, hybrid ac/dc microgrids, and high-power converters.

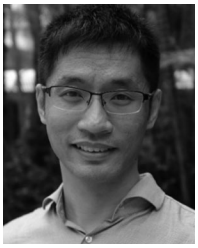

Xin Zhang (M'15) received the Ph.D. degree in automatic control and systems engineering from the University of Sheffield, Sheffield, U.K., in 2016, and the Ph.D. degree in electronic and electrical engineering from Nanjing University of Aeronautics & Astronautics, Nanjing, China, in 2014.

He is currently an Assistant Professor of Power Engineering with the School of Electrical and Electronic Engineering, Nanyang Technological University, Singapore. He was a Postdoctoral Research Fellow with the City University of Hong Kong from January 2017 to September 2017, and a Research Associate with the University of Sheffield from February 2014 to December 2016. His current research interests include power electronics, power system, and advanced control theory, together with their applications in various sectors.

Dr. Zhang was the recipient of the highly prestigious Chinese National Award for Outstanding Students Abroad in 2016. He is the Associate Editor for IEEE TRANSACTIONS ON INDUSTRIAL ELECTRONICS/JOURNAL OF EMERGING AND SELECTED TOPICS IN POWER ELECTRONICS/ACCESS and *IET Power Electronics*. He is the Committee Member of the IEEE IAS/PELS Joint Chapter at Singapore and the General Manager of Air T&D Pte Ltd, Singapore.

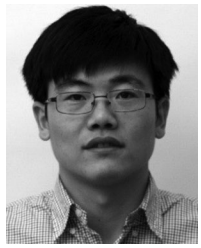

Bin Zhao (M'18) received the B.S. degree in electrical engineering from Nanjing Agricultural University, Nanjing, China, in 2012, and the Ph.D. degree from the Institute of Electronics, Chinese Academy of Sciences, Beijing, China, in 2017.

From September 2015 to December 2016, he was a Visiting Scholar with the National University of Ireland, Galway, Ireland. From January 2017 to 2018, he was a Postdoc Researcher with the Department of Electrical Engineering, Technical University of Denmark. From February 2018 to January 2019, he was a Research Fellow with Energy Research Institute @ NTU, Nanyang Technological University. Since January 2019, he has been with Space Travelling-Wave Tube Research & Development Center, Institute of Electronics, Chinese Academy of Sciences, Beijing, China, as a Research Professor. His current research interests include high-frequency magnetic simulation, design, and integration in power electronics and resonant converters.